Dependence of critical current density on microstructure in the SnMo$_6$S$_8$ Chevrel phase superconductor

L. A. Bonney,[a] T. C. Willis,[b] and D. C. Larbalestier[b]
Applied Superconductivity Center, University of Wisconsin—Madison, 1500 Johnson Drive, Madison, Wisconsin 53706

Microstructure and superconducting properties of hot isostatic pressed SnMo$_6$S$_8$ were systematically studied. Magnetization was measured in fields up to 30 T at 4.2–14 K. SnMo$_6$S$_8$ exhibits critical current densities limited by flux pinning, not by granularity. Samples exhibited $B_{irr}(T)$ ~ $B_{c_2}(T)$, indicative of strong flux pinning. Pinning force curves contained two distinct peaks, indicating that at least two pinning mechanisms are active. The microstructure contained two types of defects which could pin flux: grain boundaries and planar intragranular defects. Lower-field pinning ($B/B_{c_2} \lesssim 0.3$) was directly correlated to the grain boundary density. Higher-field pinning ($B/B_{c_2} \gtrsim 0.5$) appeared to be controlled by the intragranular pins. Compared to Nb$_3$Sn, the grain sizes are large and the contribution from grain boundary pinning is small. Inhibiting grain growth through lower-temperature processing and increasing the density of intragranular defects both appear feasible means of further increasing J_c. © 1995 American Institute of Physics.

I. INTRODUCTION

Chevrel phase (CP) superconductors are of interest for magnet applications at fields greater than 20 T, because of their high upper critical field, B_{c_2}, values: B_{c_2}(4.2 K)>50 T for PbMo$_6$S$_8$ (PMS) and B_{c_2}(4.2 K)>30 T for SnMo$_6$S$_8$ (SMS). This high B_{c_2} and the relative strain insensitivity[1] of their critical current densities, J_c, make CP materials strong potential competitors for Nb$_3$Sn. Their nearly isotropic crystal structure and superconducting properties give them the advantage of not needing to be textured, as do high-temperature superconductors (HTS). For practical application, Chevrel phase J_c values in excess of 5×10^8 A/m^2 are needed to generate fields in excess of 20 T.[2] Kubo *et al.* recently achieved J_c(20 T)~1.5×10^8 A/m^2 in a PbMo$_6$S$_8$ wire, and a small coil wound from this wire achieved 84% of short sample J_c.[3] This J_c is on the order of the highest reported for CP wires but is still two orders of magnitude lower than expected for PbMo$_6$S$_8$ based on theoretical calculations.[4] The reasons for the comparatively low J_c values are debated because the mechanisms that control J_c in these materials are still not well understood. Weak-link behavior has been reported in some CP samples;[5,6] however, it is now clear that when the samples are well consolidated by hot isostatic press (HIP) processing, bulk critical currents are not percolative.[6,7] Thus, barring extrinsic limitations, such as nonuniform cross section, or intrinsic limitations, such as deviations from ideal chemistry, J_c should be controlled by the pinning of flux at microstructural defects. Flux pinning at grain boundaries is consistent with the grain size dependence of J_c observed in PbMo$_6$S$_8$ samples prepared by differing methods.[8–10] Neutron irradiation of PbMo$_6$S$_8$ enhances J_c.[9] It was also observed that a single crystal of SnMo$_6$S$_8$ exhib-

ited anomalous field-dependent magnetization characteristic of weakly superconducting pins.[11] These pins are of necessity intragranular pins. These differing sets of results all suggest that flux pinning occurs both at grain boundaries and at intragranular defects in Chevrel phase superconductors.

In view of these diverse pinning possibilities, it is a little surprising that higher J_c values have not been obtained, since there appears to be no obvious barrier to raising the J_c values at comparable reduced values of $b = B/B_{c_2}$ to values seen in the A15 compounds. The goal of our study was to explore this question. This article reports on the high-field flux pinning in polycrystalline SnMo$_6$S$_8$ bulk samples which were carefully prepared so as not to exhibit evidence of poor connectivity. To this end bulk SnMo$_6$S$_8$ material was consolidated by HIP processing and then divided into multiple samples which were given various thermal treatments designed to promote grain growth. Systematic study of the microstructure and the J_c of these samples over a wide region of temperature and field space was undertaken in order to identify the flux pinning centers and flux pinning mechanisms.

II. EXPERIMENTAL METHODS

The microstructure of HIP-treated SnMo$_6$S$_8$ was systematically modified, and the corresponding microstructure and superconducting properties were examined. Because the T_c of SnMo$_6$S$_8$ is sensitive to degradation by oxygen[12,13] and carbon[14] additions, materials were handled in an inert N$_2$/Ar atmosphere and heat treated in a partial pressure of Ar or under a vacuum of <5×10^{-6} Torr in quartz encapsulation tubes. The SnMo$_6$S$_8$ was prepared from elemental powders. Submicron Mo powder (of 99.8% purity) was reduced under flowing H$_2$ at 1000 °C in order to remove adsorbed oxygen. Sn powder of 200 mesh ($\leq$100 μm) size and 99.995% purity, and S powder of 99.999% purity were used. The powders of Sn, Mo, and S were mixed in a stoichiometric ratio of 1:6:8, cold isostatically pressed (CIP'ed), and reacted for 20 h at

TABLE I. Heat treatment, microstructure, and superconducting properties of each $SnMo_6S_8$ sample are as follows: temperature (T) and time (t) of post-HIP thermal treatments (all samples were first HIP'ed at 800 °C for 8 h), grain boundary length per unit area (L_{gb}), onset T_c (T_{con}), transition width (ΔT_c), irreversibility field (B_{irr}), upper critical field (B_{c_2}) and magnetization-derived J_c.

Sample name	Heat treatment		L_{gb} (μm^{-1})	T_c (K)		B(4.2 K) (T)		J_c(4.2 K) [A/mm^2]			
	T (°C)	t[h]		T_{con}	ΔT_c	B_{irr}	B_{c_2}	5 T	10 T	15 T	20 T
T0	···	···	4.0±0.6	14.3	<0.2	26.7	29.0	1570	770	420	160
T1	1000	20	3.6±0.6	14.3	<0.2	25.0	28.0	1230	640	360	90
T2	1000	100	3.3±0.5	13.3	0.8	···	···	990	400	···	···
T3	1150	50	2.3±0.4	13.6	0.3	···	···	680	460	···	···
T4	1150	250	2.1±0.2	14.3	0.3	25.9	28.3	630	520	410	130

420 °C. The temperature was then increased over 10 h to 530 °C and held until only gray or black powders, presumably MoS_2, SnS, and Mo, were observed. These powders were ground, CIP'ed, wrapped in Mo foil, and reacted for 100 h at 800 °C to form the Chevrel phase. For this and subsequent thermal treatments, an oxygen getter of Y_2S_3 wrapped in Mo foil was used. The $SnMo_6S_8$ compact was reground to a powder, CIP'ed, wrapped in Mo foil, encapsulated under a vacuum of $<5\times10^{-6}$ Torr in stainless steel, and HIP'ed for 8 h at 800 °C under 2 kbar of Ar. This monolithic piece of $SnMo_6S_8$ was then cut into several smaller samples for the post-HIP thermal treatments.

Microstructure was studied by x-ray diffractometry (XRD), by scanning electron microscopy (SEM), and by conventional and high-resolution transmission electron microscopies (CTEM and HRTEM). Powdered samples were studied by XRD to identify the phases present. Bulk samples were metallographically polished and observed by SEM in both secondary (SEI) and backscattered (BEI) electron imaging modes so as to emphasize surface morphology and atomic number contrast, respectively. For TEM examination, wafers of each sample were metallographically polished and then ion thinned to electron transparency. Grain morphology and microstructural defects were observed by CTEM. Local chemistry was probed by energy-dispersive x-ray spectroscopy (EDX) in both the SEM and the TEM. Grain boundaries were traced from transmission electron micrographs and grain boundary length per unit area, L_{gb}, was measured by image analysis of the tracings. Grain boundaries and intragranular defects were examined more closely by HRTEM.

The superconducting transition temperature, T_c, was measured by ac susceptometry in a 103 Hz ac field of 940 μT, zero-to-peak. The magnetic field and temperature dependence of the superconducting critical current density, J_c, was systematically examined by vibrating sample magnetometry (VSM). By this technique, magnetic moment was measured, first, in our laboratory at temperatures between 4.2 and 14 K in fields between 0 and 12 T and, later, at the Francis Bitter National Magnet Laboratory at temperatures between 4.2 and 14 K and in dc fields between 0 and 20 T and at 4.2 K between 0 and 30 T. Samples were parallelepipeds, typically 1–3 mm on a side. J_c was calculated from:

$$J_c = \frac{3\Delta m}{V\ell},$$
(1)

where Δm is the hysteresis in moment between increasing and decreasing field and V is the sample volume. The scaling length ℓ was calculated from:

$$\ell = \frac{3}{2}\ell_1\left[1 - \frac{\ell_1}{3\ell_2}\right],$$
(2)

where ℓ_1 and ℓ_2 are the smaller and larger dimensions, respectively, of the sample in the plane perpendicular to the magnetic field.

B_{irr} and B_{c_2} values were determined from the magnetization curves. B_{irr} was determined from the intersection of the extrapolations of the field-increasing and field-decreasing irreversible magnetization loops. The transition at B_{c_2} occurred at somewhat higher fields (about 1 T higher at 4.2 K) and manifested itself by a sharp change of slope in the reversible M-B curve.

III. RESULTS

Samples were studied in five post-HIP conditions as specified in Table I: in the as HIP'ed condition (8 h at 800 °C and 2 kbar) (T0); annealed 20 h at 1000 °C (T1); annealed 100 h at 1000 °C (T2); 50 h at 1150 °C (T3); and annealed 250 h at 1150 °C (T4). Increasing sample number indicates that an increasingly aggressive thermal treatment was given in order to provoke grain growth.

A. Microstructural characterization

XRD analyses indicated that small quantities of second phases were present in these samples. Mo was detected in samples T0, T1, and T3, and MoS_2 was also detected in T0 by XRD. By BEI in the SEM, three distinct phases were observed: the majority $SnMo_6S_8$ phase, a brighter (higher atomic number) phase, and a darker (lower atomic number) phase (Fig. 1). All of the samples were observed to contain less than 5 vol % of these phases. The second phase content decreased markedly as the thermal treatment was increased. EDX analysis of the brighter phase indicated that Mo, and possibly S, were present in the phase. Unfortunately, the relative amounts of Mo and S in each phase could not be distinguished by EDX, because of the energy overlap of the S-K_α x-ray peak with the Mo-L_α x-ray peak. However, because no molybdenum or tin sulfide compound has a higher
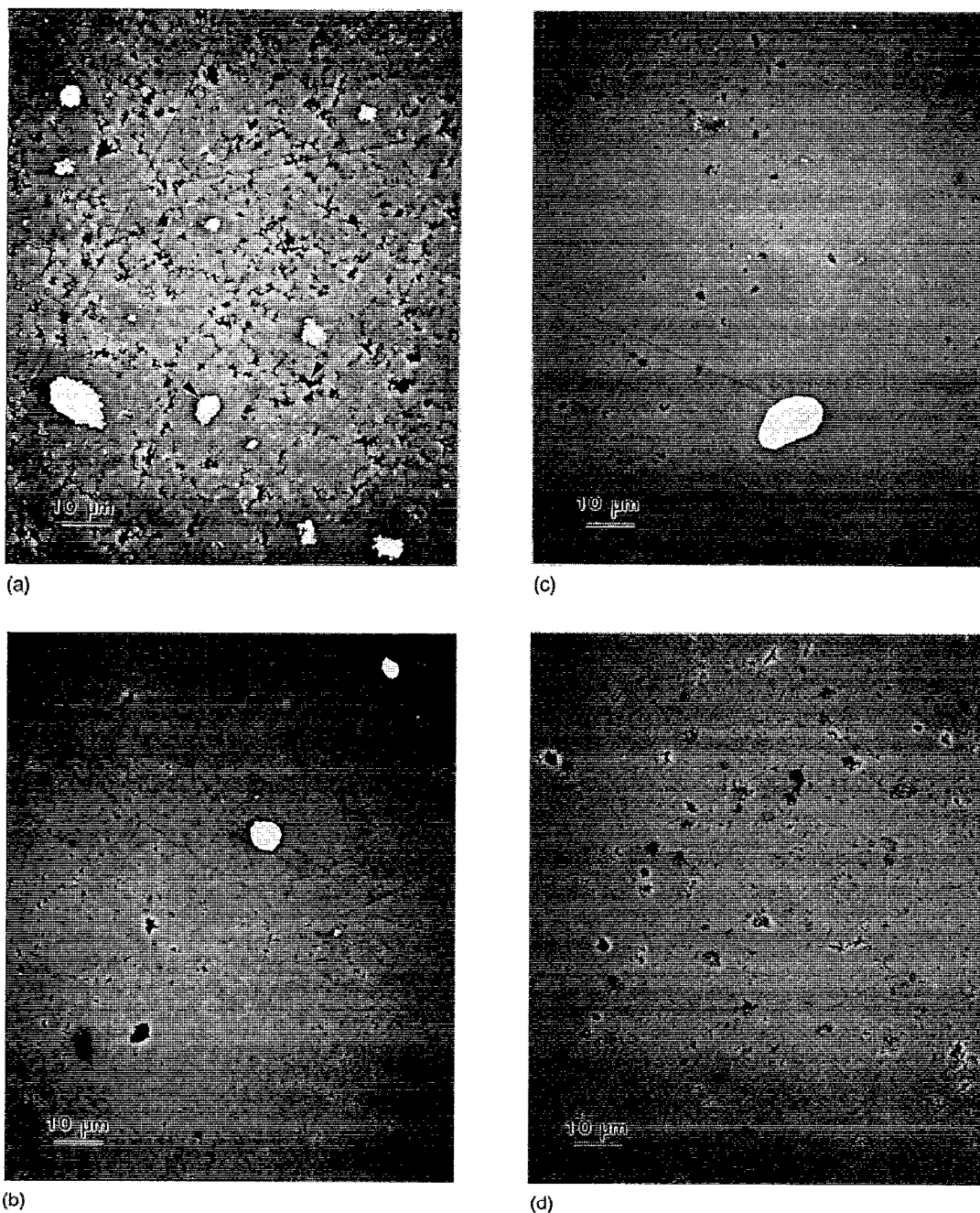
FIG. 1. Backscattered electron images (BEI) taken in the SEM of samples (a) $T0$, (b) $T1$, (c) $T2$, and (d) $T4$. Three phases are apparent: (1) the majority phase, $SnMo_6S_8$, (2) a brighter, higher average atomic number phase, Mo, and (3) a darker, lower average atomic number phase, which was identified as MoS_2 in samples treated at $\leqslant 1000$ °C and as MoS_2 or Mo_2S_3 in samples treated at 1150 °C.

average atomic number than $SnMo_6S_8$, this brighter phase is believed to be Mo. The phase that appeared darker in BEI appeared layered in the samples heat treated at $\leqslant 1000$ °C but was too small to identify by EDX in the SEM. This phase is believed to be MoS_2 because MoS_2 was detected in sample $T0$ by XRD and because this compound has a layer structure. In samples annealed at 1150 °C, the darker regions appeared to be mostly depressions in the samples' surfaces where another phase had polished away preferentially. This dark phase was assumed to be a molybdenum sulfide, MoS_2 or Mo_2S_3.

By TEM examination, grain boundaries, intragranular defects, and second phase precipitates were observed (Fig. 2). A layered second phase was observed in the samples heat treated at $\leqslant 1000$ °C ($T0,T1,T2$). By EDX analysis in the TEM, Mo was detected in this phase but, again, it was not possible to confirm or deny the presence or absence of S. The layered nature of the phase and the EDX results do support its identification as MoS_2. The second phases were not identified by TEM in the samples annealed at 1150 °C ($T3,T4$).

In both TEM and HREM micrographs, grain boundaries appeared clean of second phase and the grains well con-
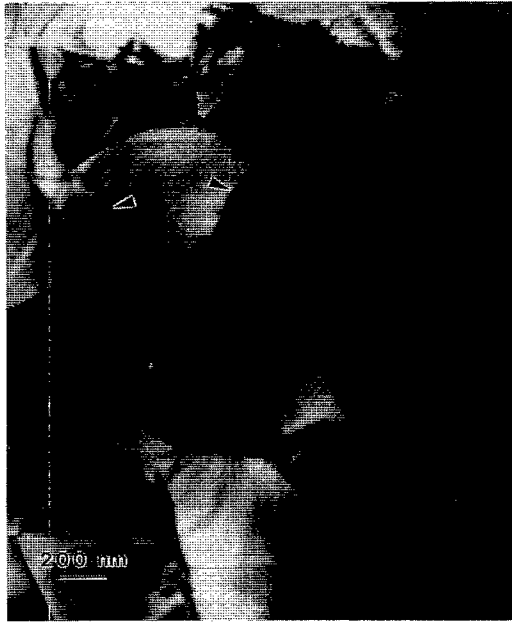
J. Appl. Phys., Vol. 77, No. 12, 15 June 1995

Bonney, Willis, and Larbalestier   6379

FIG. 2. TEM micrograph of $T4$ showing well-connected grains (arrow on the right) and planar intragranular defects (arrow on the left).

FIG. 3. HRTEM micrograph of planar defects in $T4$.

nected. Although the actual grain size ranged widely, from 20 nm to 2 μm in all samples, it was readily apparent that the overall grain size increased and, thus, grain boundary density decreased, with increasing thermal treatment. The quantitative measurements reported in Table I show that L_{gb} decreased with increasingly aggressive thermal treatment from $\sim$4 to $\sim$2 μm^{-1}. Although it was apparent from visual comparison of the TEM micrographs that grain size increased with thermal treatment, no trend in the density of intragranular defects was apparent.

Especially notable amongst the intragranular defects was a multitude of planar intragranular defects such as twins and stacking faults. An example of some of these defects is shown in Fig. 3. The length of planar defects ranged from <10 nm to the entire length of the grains containing them. Varying amounts of lattice distortion are associated with these defects. Some defects appear not to distort the lattice beyond a few atomic spacings, while others distort the lattice for 5 nm or more.

B. Electromagnetic characterization

Values for T_c onset (T_{con}) were taken as the temperature at which the susceptibility, χ_{ac}, deviated from zero. The transition width ΔT_c was estimated as the temperature difference between 10% and 90% of full screening. Both values are reported in Table I. Samples $T0$, $T1$, and $T4$ all had T_{con} values of 14.3 K, while $T2$ and $T3$ had values of 13.3 and 13.6 K. ΔT_c was <0.3 K for all samples except $T2$, which had a rather broad transition of 0.8 K. The ac susceptibility of each sample was relatively insensitive to small variations of the applied field in the low-field range, below 1 mT.[15] Because of our concern that samples $T2$ and $T3$ had some oxygen contamination, the majority of our study focussed on
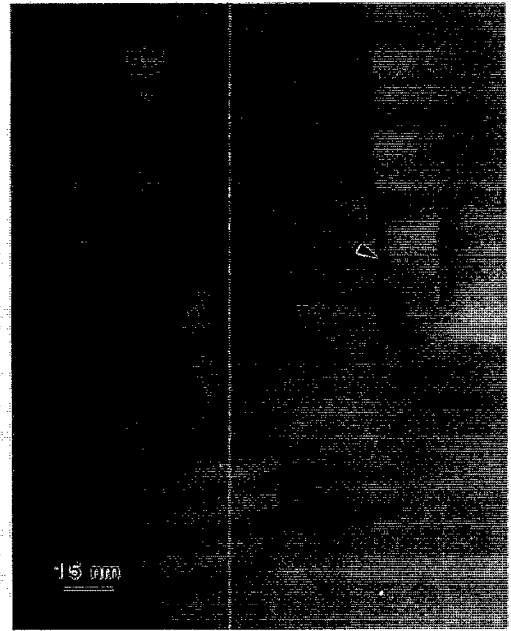
the samples $T0$, $T1$, and $T4$ which had high T_c values of 14.3 K, which is characteristic of uncontaminated SMS.

From magnetization curves the irreversibility and upper critical fields, B_{irr} and B_{c_2}, were determined from loop closure and from the slope change at the end of the reversible diamagnetic magnetization that follows loop closure, respectively, as shown in Fig. 4. Upper critical field values of the three samples having $T_c = 14.3$ K ranged between 28 and 29 T at 4.2 K. These values are listed in Table I. The values of B_{irr} and B_{c_2} are plotted in Fig. 5. They appear not to depend significantly on thermal treatment, and there is little difference between B_{irr} and B_{c_2}.
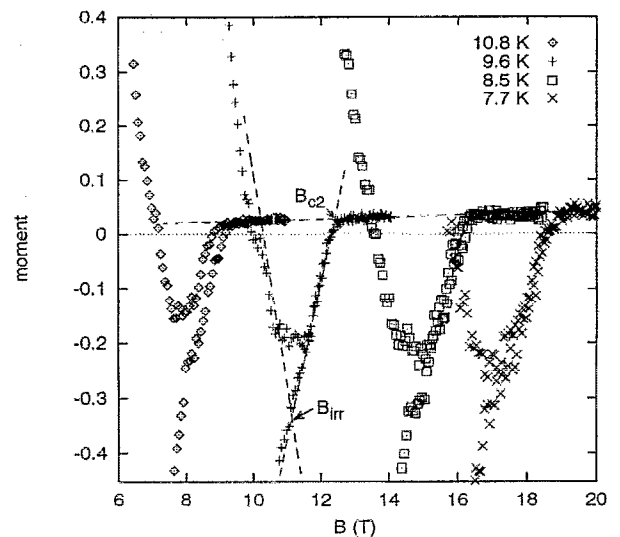

FIG. 4. Magnetization curves of $T0$ measured at different temperatures show loop closure, B_{irr}, and slope change, B_{c_2}.
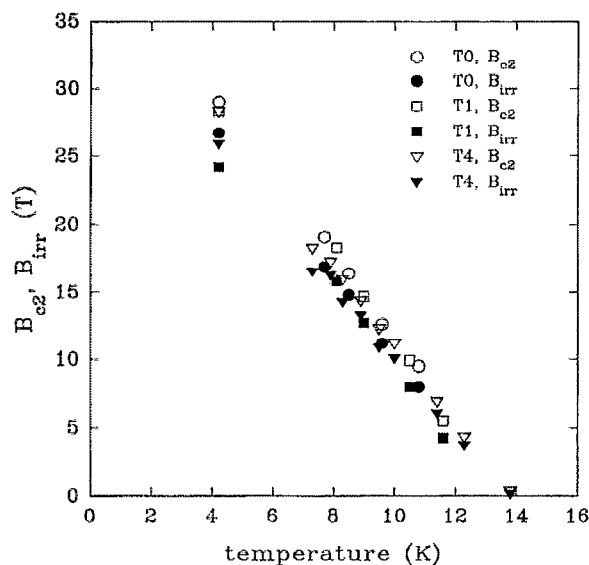
Bonney, Willis, and Larbalestier

FIG. 5. Field of loop closure B_{irr} and field of slope change B_{c_2} as a function of temperature.

FIG. 7. $J_c(B)$ dependence on grain boundary line length per unit area, L_{gb}. The lower field $J_c(\leqslant 10\ T)$ increases linearly with L_{gb}, while the higher field $J_c(\geqslant 15\ T)$ appears independent of grain size. $J_c(10\ T)$ is depressed in the samples $T2$ and $T3$ which correlates to their depressed T_c values.

The magnetization $J_c(4.2\ K)$ values are plotted in Fig. 6, and values at 5, 10, 15, and 20 T are tabulated (Table I). Flux jumping was observed for fields $\leqslant 2$ T, but these effects were smoothed out of the curves in the data analysis. The highest J_c values were 770 A/mm^2 at 10 T and 160 A/mm^2 at 20 T. Note that the lowest temperature processing led to the highest J_c over the entire field range. As the thermal treatment became more aggressive, the low-field J_c dropped significantly while the high-field J_c remained approximately constant. $J_c(4.2\ K)$ values at 5, 10, 15, and 20 T are plotted as a function of L_{gb} in Fig. 7. As reported in earlier work,[15] J_c decreases with decreasing L_{gb} at lower fields ($\leqslant 10$ T). Note

that $J_c(10\ T)$ is depressed in the samples with depressed T_c. At 15 and 20 T, J_c is independent of grain size.

Bulk pinning force density, $F_p(4.2\ K)$, as a function of field is plotted in Fig. 8. This plot makes it clear that the effect of thermal treatment is very pronounced only below $B/B_{c_2} \sim 0.4$. Consequently, the peak in the pinning force curve shifts to higher fields as the thermal treatment increases. Pinning force as a function of field for sample $T0$ at different temperatures is shown in Fig. 9(a); the data is shown in Fig. 9(b) but with F_p and B normalized to the peak pinning force, $F_{p_{max}}$, and to B_{irr}, respectively. Note that there is reasonable evidence for temperature scaling at higher temperatures ($\geqslant 10$ K), but that at lower temperature (e.g., 4.2 K)
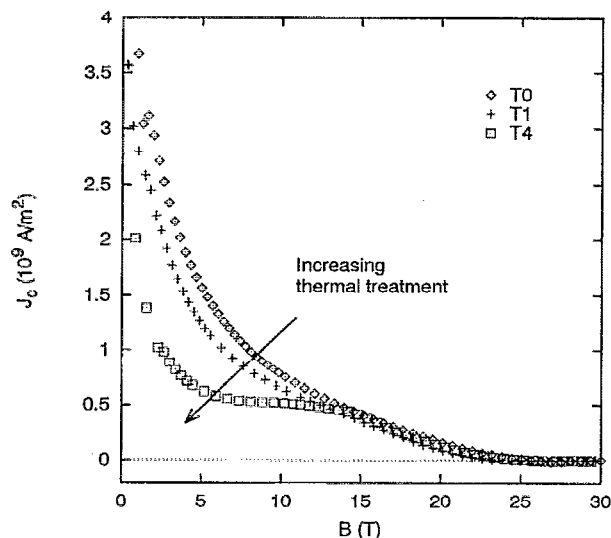

FIG. 6. Magnetization J_c measured at 4.2 K between 7 and 30 T at Francis Bitter National Magnet Laboratory (FBNML). Curves are comprised of low-field data from UW measurements (see Ref. 15) and high-field data from FBNML measurements. Low-field J_c decreases with increasing thermal treatment while high-field J_c remains nearly constant.
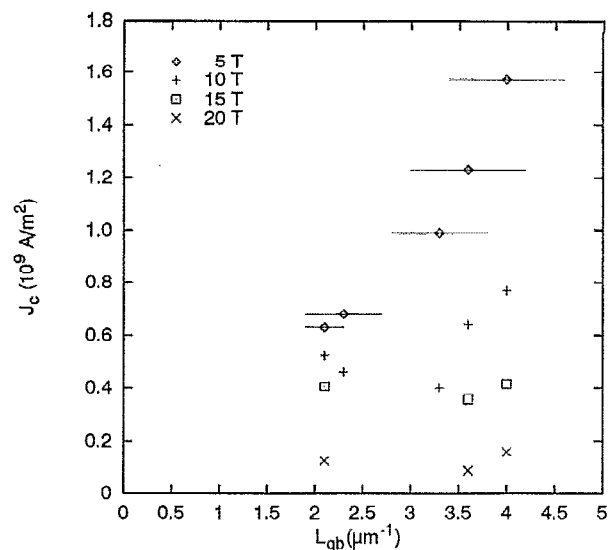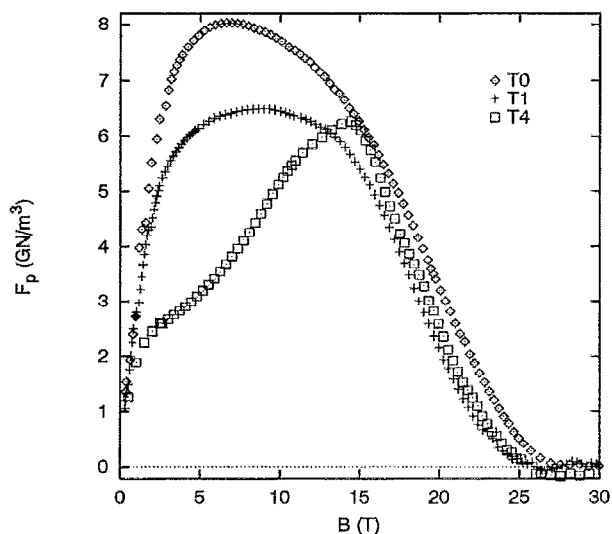

FIG. 8. Bulk pinning force F_p at 4.2 K for samples $T0$, $T1$, and $T4$. Low-field $F_p(4.2\ K)$ is depressed with increasing thermal treatment, while the high-field $F_p(4.2\ K)$ remains almost constant.
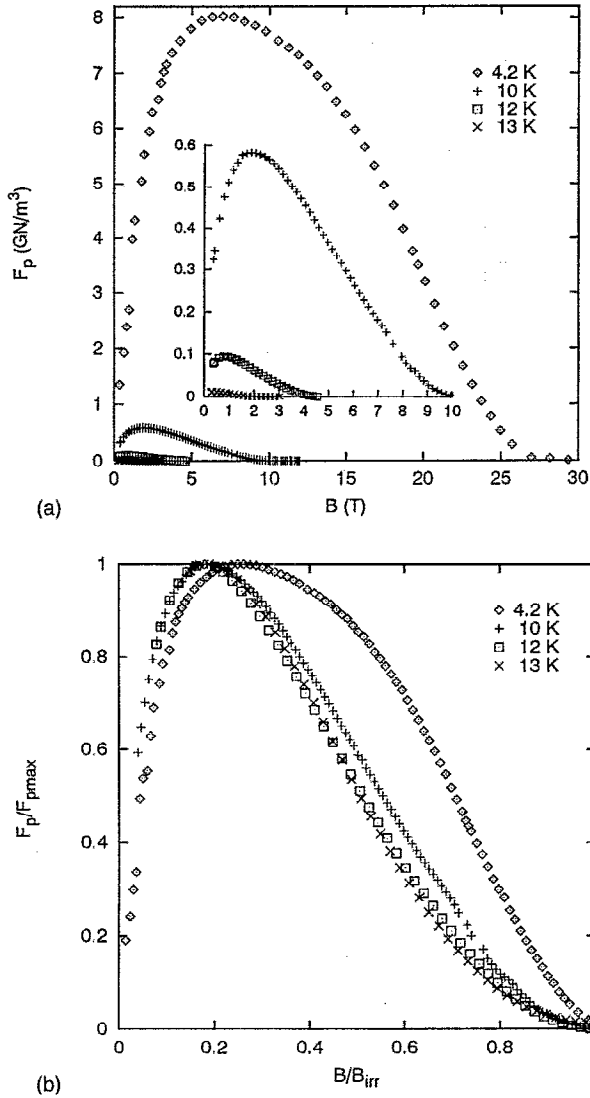
FIG. 9. (a) $F_p(T)$ for $T0$ at 4.2, 10, 12, and 13 K. (b) Reduced pinning force as a function of reduced field for $T0$. Pinning force scales at higher temperatures but a peak shift is observed at 4.2 K.

FIG. 10. (a) $F_p(T)$ for $T4$ at 6.6, 7.9, 8.9, 10, 11.4, and 12.3 K shows high-field F_p decreasing more rapidly than low-field F_p. (b) Reduced pinning force as a function of reduced field for $T4$ at the same temperatures in (a), as well as at 4.2 K. Observe that the data falls on two curves, one peaking at low fields at higher temperatures, and one peaking at higher fields at lower temperatures.

a high-field bulge develops above B_{max}, the field of maximum pinning force. Similarly, Fig. 10(a) and 10(b) show pinning force and normalized pinning force data at different temperatures for sample $T4$. Note that the high-field pinning force diminishes with increasing temperature more rapidly than does the low-field F_p. In this sample there is an apparent trade off between two peaks, one having its maximum at $\sim 0.1 B_{irr}$ and the other at $\sim 0.5 B_{irr}$; there is a continuous relative shift in the location of maximum pinning from higher fields to the lower fields as the temperature increases. Thus, a positive effect is that the high-field pinning contribution is maximized at lower temperatures.

C. Modeling of pinning force curves

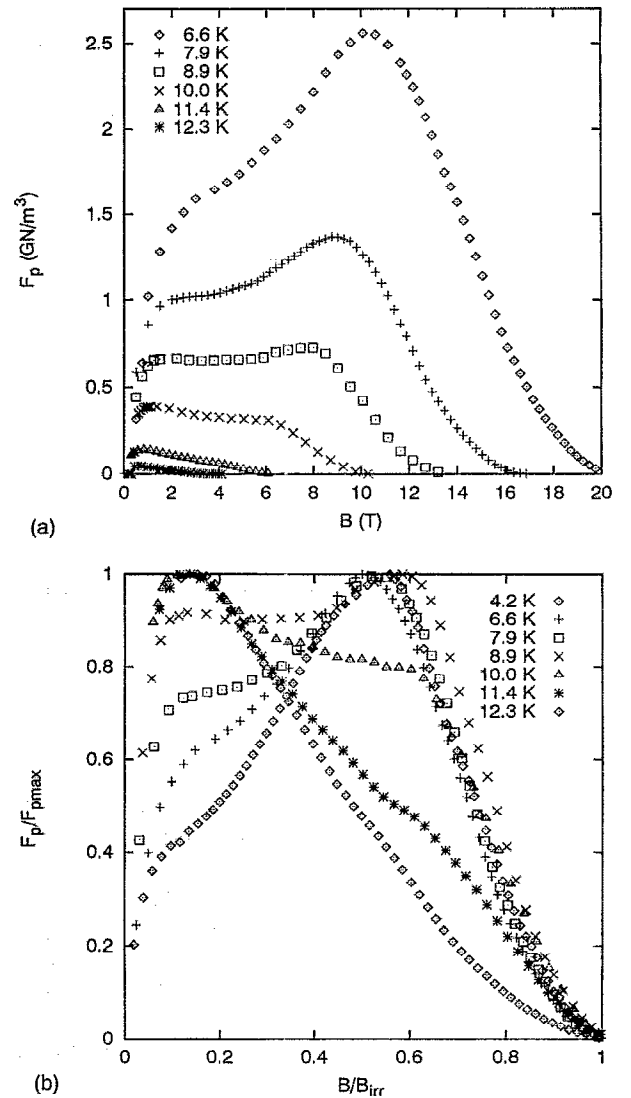Because of the observed grain size dependence of J_c, at least at low fields, Kramer plots were made of the data, as is commonly done for Nb$_3$Sn, for which grain boundary pinning is well established (Fig. 11). The Kramer model[16] predicts that

$$F_p \propto \frac{B_{c_2}^{5/2} b^{1/2} (1-b)^2}{\kappa^2 (1-a_0 \sqrt{\rho})^2}, \qquad (3)$$

where b is B/B_{c_2}, κ is the Ginzburg–Landau parameter, a_0 is the interfluxon spacing, and ρ is the density of pinning centers. Assuming that $a_0 \sqrt{\rho} \ll 1$, which is the case at fields >5 T in these materials, algebraic manipulation of Eq. (3) gives

$$J_c^{1/2} B^{1/4} \propto (B_{c_2} - B)/\kappa. \qquad (4)$$

Linear extrapolation of $J_c^{1/2} B^{1/4}$ versus B (the Kramer plot) should then give B_{c_2}. It is apparent from Fig. 11 that the
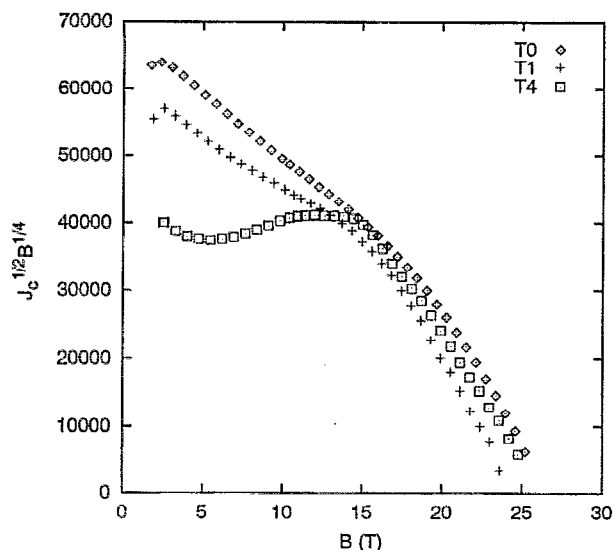
FIG. 11. Kramer plots for samples $T0$, $T1$, and $T4$. Data is not well described by the Kramer model.

Kramer model provides a significantly worse description of the data than is normally observed in Nb_3Sn.

Because the experimental $F_p(B)$ curves tended to exhibit a bimodal function, pinning forces were fit[17] as the sum of two curves of function:

$$F_p \propto b^p (1-b)^q, \tag{5}$$

where $b = B/B_{irr}$ and p and q are variable parameters. The 4.2 K pinning force curves were first fit to $b^{1/2}(1-b)^2$ and $b(1-b)$, because these are $F_p(B)$ functions commonly observed in Nb_3Sn and Nb-47 wt. % Ti (Nb-Ti), respectively. The correlation coefficients of these fits decreased from 99% for $T0$ to 85% for $T4$, as shown in Fit A of Table II. Figure 12 shows the two fits and their sum superimposed on the data for each sample. Although the fit is excellent for sample $T0$, the fit for $T4$, which has pronounced bimodal $F_p(B)$, does not represent the data at all. The pinning force data was next fit to $b^{1/2}(1-b)^2$, the $F_p(B)$ dependence characteristic of grain boundary pinning, and $b^p(1-b)^q$, where p and q were left as free parameters. The results are shown as Fit B in Table II. In this case, the correlation coefficients were all >99%. For all samples in Fit B, the position of the pinning force maximum, $b_{max} = B_{max}/B_{irr}$, is $b_{max} = 0.5-0.6$ for the high-field peak. The peak pinning force and the relative area under the curve, A_{F_p}, declines with decreasing L_{gb} for the

low-field fit, while A_{F_p} remains constant within 25% for the high-field curves. All of this is consistent with there being one low-field pinning mechanism which is strongly dependent on thermal treatment and one high-field pinning mechanism which is relatively independent of treatment.

If two functions of the type $F_p \propto b^p(1-b)^q$ were chosen, such that one had $b_{max} \sim 0.1$ and the other $b_{max} = 0.5-0.6$, then the $F_p(B)$ data for all samples at all temperatures could be fit to >99% correlation. Whatever fit functions were used, it is clear that $F_p(B)$ for all samples is comprised of two curves of nominally the same functional dependence and that the low-field curve is similar to the $F_p(B)$ of grain boundary pinning observed in Nb_3Sn.

IV. DISCUSSION

A. Sample quality

Although these samples were carefully prepared and given extensive heat treatments, it is apparent from SEM and TEM that they were not completely single phase. The presence of free Mo suggests that the samples were not quite completely reacted. A few percent (always <5%) molybdenum and molybdenum sulfide second phases of a few microns or less diameter were present in all samples. We do not consider that these exerted any significant flux pinning role, since their size was typically $10^3 \xi(4.2 \text{ K})$, where ξ is the Ginzburg–Landau coherence length. By contrast, the superconducting $SnMo_6S_8$ phase had a wide range of grain sizes and contained many intragranular defects, the characteristic size of which is suitable for flux pinning.

These samples exhibited some of the highest J_c values reported for Chevrel phase materials. Samples $T0$, $T1$, and $T4$ had high critical temperatures and upper critical fields. We believe that $T2$ and, to a lesser extent, $T3$ were contaminated with oxygen during heat treatment; this is consistent with their depressed T_c values and the broad T_c transition of $T2$. Low-field ac susceptibility measurements showed that these samples were not granular, as did comparison of $J_c(\Delta M)$ versus $J_c(\Delta H)$.[15] In both TEM and HREM micrographs, grains appeared well connected. Thus, based on microstructural and electromagnetic results, we are confident that we are studying flux pinning effects in well-coupled samples, not granular and/or percolative effects in poorly connected or weakly coupled samples.

In summary, we do not believe that these large second phase particles significantly contributed to the observed flux

TABLE II. Fit parameters from modelling of pinning force curves as $C_1 b^{p_1}(1-b)^{q_1} + C_2 b^{p_2}(1-b)^{q_2}$.

Fit	Sample name	Low-field peak						High-field peak						Corr. coef.
		C	p	q	b_{max}	$F_{p_{max}}$	A_{F_p}	C	p	q	b_{max}	$F_{p_{max}}$	A_{F_p}	
A	$T0$	2.6	0.5	2	0.2	6.0	3.2	1.5	1	1	0.5	3.0	2.0	>0.99
	$T1$	2.3	0.5	2	0.2	4.3	2.3	2.0	1	1	0.5	3.2	2.2	0.98
	$T4$	0.5	0.5	2	0.2	0.94	0.49	2.9	1	1	0.5	4.5	3.0	0.85
B	$T0$	2.8	0.5	2	0.2	6.5	3.5	2.9	1.6	1.4	0.53	2.9	1.7	>0.99
	$T1$	3.0	0.5	2	0.2	5.6	3.0	14	2.9	2.1	0.58	2.9	1.4	>0.99
	$T4$	1.5	0.5	2	0.2	2.8	1.5	97	4.0	3.1	0.56	4.6	1.9	>0.99

J. Appl. Phys., Vol. 77, No. 12, 15 June 1995

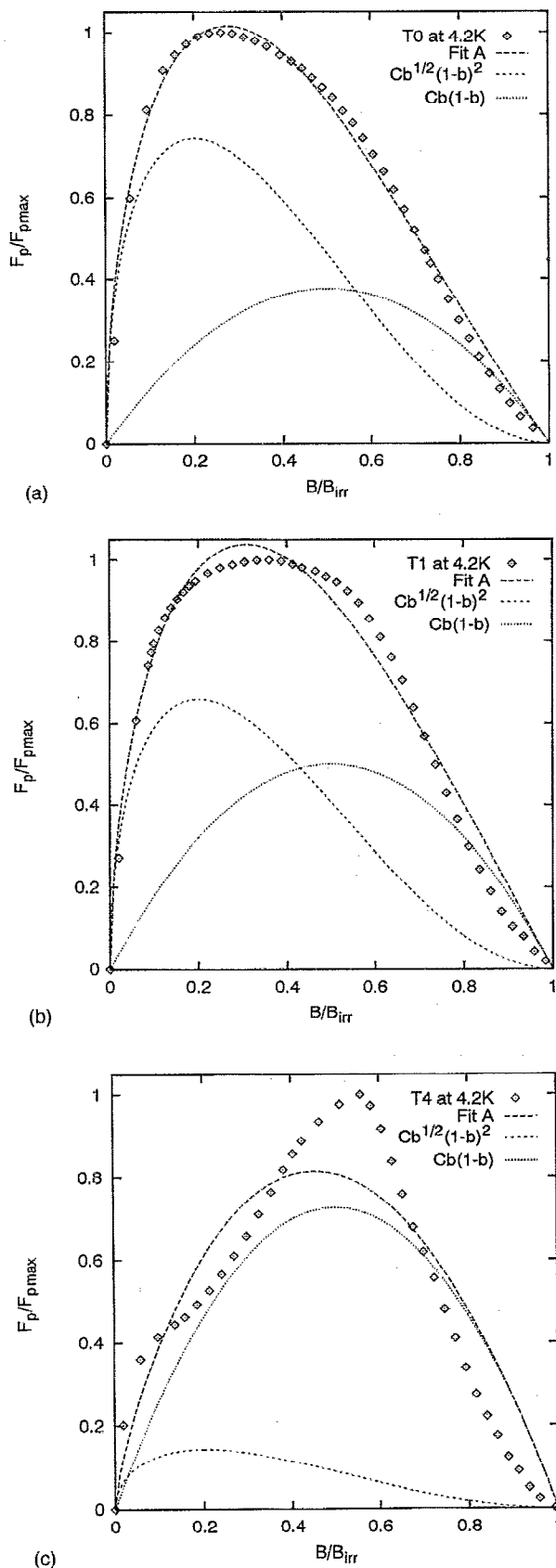Bonney, Willis, and Larbalestier   6383

(a)

(b)

(c)

FIG. 12. Pinning force curves of (a) $T0$, (b) $T1$, and (c) $T4$ at 4.2 K fit to $C_1 b^{1/2}(1-b)^2 + C_2 b(1-b)$. The points represent data and lines are the 2 curves and their sum which is fit to the data. The fit to $T0$ is good but the fit becomes increasingly poor as thermal treatment increases.

pinning. We believe that the grain boundaries and the planar intragranular defects are the microstructural features having the size and density responsible for the observed flux pinning in these materials.

B. Flux-pinning characteristics and correlation to microstructure

Examination of the magnetization curves shows that J_c goes to zero only very close to B_{c_2}. That $B_{irr}(T)$ is close to $B_{c_2}(T)$ in these SnMo$_6$S$_8$ samples is consistent with the results of Suenaga et al. for PbMo$_6$S$_8$, Nb-Ti, and Nb$_3$Sn, and contrasts strongly with results for the high-temperature superconductors (HTS) YBa$_2$Cu$_3$O$_{7-\delta}$, Bi$_2$Sr$_2$CaCu$_2$O$_8$, and Bi$_2$Sr$_2$Ca$_2$Cu$_3$O$_{10}$.[18,19] Because the CP have coherence lengths intermediate between the A15 compounds and HTS compounds, it would not be surprising if some of the sensitivity to thermal activation and consequent separation of B_{irr} and B_{c_2} were also observed in high B_{c_2} CP materials, too. $\xi(4.2 \text{ K})$ for SnMo$_6$S$_8$ is about 3.2 nm and about 2.5 nm for PbMo$_6$S$_8$. Rossel et al., indeed, found that the irreversibility line was strongly depressed below $B_{c_2}(T)$ in PbMo$_6$S$_8$ single crystals.[20] The reason for this discrepancy in irreversible behavior of single crystal and polycrystalline PbMo$_6$S$_8$ is unclear, but could result from the weaker flux pinning of single crystals, as also observed by Le Lay et al.[11] As discussed by Suenaga et al.,[18,19] the observed irreversibility line could result from the thermally activated depinning of fluxons or from a phase transition from a flux-line lattice or glass to a fluidlike state. They showed that both mechanisms are plausible, though imperfect, explanations for this behavior in the low-temperature superconductors Nb-Ti and Nb$_3$Sn.[18] In either case, strong flux pinning can inhibit the flux motion that leads to the irreversible behavior. Regardless of the cause of the irreversible behavior in these SnMo$_6$S$_8$ samples, the proximity of B_{irr} to B_{c_2} is evidence of strong pinning and indicates that its short coherence length poses no intrinsic barrier to the development of high J_c in CP conductors.

Although the lowest temperature processing led to the best J_c(4.2 K) values over the entire field range, the sample-to-sample variation in J_c was pronounced only at lower fields. While the lower field $J_c(B<10$ T) clearly decreased with increasing thermal treatment, the higher field $J_c(B>15$ T) was not strongly affected by the grain growth which resulted from the post-HIP anneals. The grain size dependence of J_c(4.2 K) (Fig. 7) indicates that grain boundaries are the pinning centers which control J_c below 10 T. The $b^{1/2}(1-b)^2$ dependence of the low-field component of $F_p(B)$ also strongly points to grain boundaries as the source of the low-field pinning. In Nb$_3$Sn, J_c is also grain size dependent at lower fields and independent near B_{c_2},[21] but J_c is grain-size dependent to about 0.7–0.8 B_{c_2} rather than to 0.5 B_{c_2} as observed in these SMS samples. Nb$_3$Sn samples that have been annealed to produce very large grain sizes, thus lower pin densities, have also been reported to have depressed low-field J_c values, leaving a high-field peak.[22] Nb$_3$Sn does not, however, exhibit the bimodal $F_p(B)$ curve which we observe for SMS. Consistent with this, grain

Bonney, Willis, and Larbalestier

boundaries are the only significant flux pinning center identified in bronze or internal tin route Nb₃Sn wires. SMS, on the other hand, contains both grain boundaries and intragranular defects. Consistent with the importance of intragranular defects, neither the high-field pinning nor the density of intragranular defects appeared significantly affected by the post-HIP thermal treatments. Intragranular defects are more closely spaced than grain boundaries, and fluxons are more closely spaced at higher fields. Thus, we conclude that the intragranular defects are the pinning centers responsible for the high-field pinning in these $SnMo_6S_8$ samples.

The $J_c(B)$ data in Fig. 6 is suggestive of saturation behavior (insensitivity of the high-field pinning force to microstructure) found in other materials.[22-25] Küpfer et al. showed that the peak of the $F_p(b)$ curve (b_{max}) occurs at lower fields as the defect density increased for Nb₃Sn and V₃Si samples[25] while Fig. 8 shows b_{max} falling as grain size increases in the SMS samples. Saturation can not, however, account for the bimodal nature of the $F_p(B)$ curves in the SMS samples represented in Fig. 12, nor the lack of temperature scaling found in Figs. 9(b) and 10(b).

The different field dependence and different contributions of the two flux pinning mechanisms lead to changes in the shapes of the pinning force curves, as is clear in Figs. 8–10. Somewhat similar shifts in the peak pinning force have been previously observed with varying processing temperature[26] and, to a lesser extent, with varying measurement temperature.[9,27] Bimodal $F_p(B)$ curves were observed in hot-pressed $PbMo_6S_8$ by Rossel and Fischer.[9] The bimodal nature of the $F_p(B)$ curves is consistent with the existence of more than one flux pinning mechanism or regime. F_p curves were satisfactorily modeled as the sum of two functions, a low-field and a high-field curve, which are each of nominally the same functional dependence but different magnitude for each sample and each temperature. Thus, there appears to be a pattern common to both SMS and PMS of two pinning mechanisms, one dominating at lower and one at higher fields.

C. Underlying flux-pinning mechanisms

The complexity of the pinning force curves noted above makes it difficult to construct a quantitative description of the pinning mechanisms operating in these samples. The simplest approach would be to apply full summation, but full summation of the elementary pinning forces between individual fluxons and defects seems very unlikely given the low density of observed defects which is much less than the fluxon density at almost all fields. This is consistent with the comparatively low J_c values of $SnMo_6S_8$ samples, as compared to Nb₃Sn, as we discuss further in the next section.

These findings may be considered in light of flux pinning theory. Given the influence of grain boundaries on the pinning force (Fig. 7), it is natural to consider the flux line lattice shear (FLS) model as the underlying mechanism for controlling the flux pinning. In its original form,[16] this model predicted that $F_p \propto b^{1/2}(1-b)^2$, a functional dependence which is generally observed in Nb₃Sn, where evidence for grain boundary pinning is strong.[28] It is clear from Fig. 11 that the same function does not fit the present data. Since

Kramer's original formulation, there have been several attempts to test the predictions of the original FLS model. Suenaga and Welch[29] pointed out that, although the model correctly linearizes the J_c data using the function $J_c^{1/2}B^{1/4} \propto (1 - B/B_{c_2})$, the κ dependence is opposite to predictions. Wördenweber[30] further developed the model for the case of thin films with inhomogeneities within the two-dimensional limit and found greater flexibility in pinning force curve shape than in the original model. Matsushita and Küpfer attributed depressed low-field J_c to saturation of the pinning sites by the available fluxons in the limit of low pin density.[24] In the case of the present data, grain boundary density was reduced by increasing thermal heat treatment. However, we must assume that the intragranular defect density was not reduced by the same treatments.

A more general view is provided by collective pinning theory[31] which may account, at least qualitatively, for the present situation, in which we think that there are at least two pin types: grain boundaries and intragranular defects. Collective pinning considers pinning of fluxons to occur in correlated bundles rather than individually and applies to systems having a high density of weak pins. This would describe intragranular pinning. Considering the present data in light of collective pinning, we calculated the critical distance (R_c) over which there should be short-range order transverse to the flux line from

$$R_c = 32^{1/2} \frac{C_{66}^{3/2} C_{44}^{1/2} a^{1/2}}{nf^2} = \left[\frac{2aC_{66}}{BJ_c}\right]^{1/2}, \qquad (6)$$

where a is the flux-line lattice (FLL) parameter, n is the density of pinning centers, and f is the force of interaction of an individual pinning center with the FLL. C_{44} and C_{66} are the tilt and shear moduli of the FLL, where, assuming $\kappa \gg 1$,

$$C_{66} \approx \frac{B_{c_2}^2}{\mu_0} \frac{b(1-b)^2}{8\kappa^2} (1 - 0.29b). \qquad (7)$$

For $T0$ at 4.2 K, we find that R_c is ~0.4 μm and varies only weakly with field (by less than a factor of 1.5) and that R_c is comparable to, but larger than, the size of most grains in this sample (Fig. 13). On the other hand, R_c values calculated for $T4$ at 4.2 K are about twice as large, which is greater than the average grain size (d) at fields <10 T. However, R_c does become less than the average grain size at >10 T. At higher temperatures (e.g., 10 K), R_c increases to ≥1 μm, as compared to d, which varies from 1/4 to 1/2 μm. Within the framework of collective pinning, it is possible to conceive of two flux pinning regimes. One occurs at lower temperatures, where intragranular pinning becomes significant because the correlated volume is smaller than most grains, and one at higher temperatures where both intragranular defects and grain boundaries fall within each correlated volume. As the average grain size increases over the sample set in going from $T0$ to $T4$, intragranular pinning should contribute more strongly to the bulk pinning force F_p at any given measurement temperature (below T_c), and intragranular pinning should be a stronger factor in determining F_p to higher measurement temperatures in the samples with larger d. Thus, grain boundary pinning dominates at the smaller grain sizes,

J. Appl. Phys., Vol. 77, No. 12, 15 June 1995

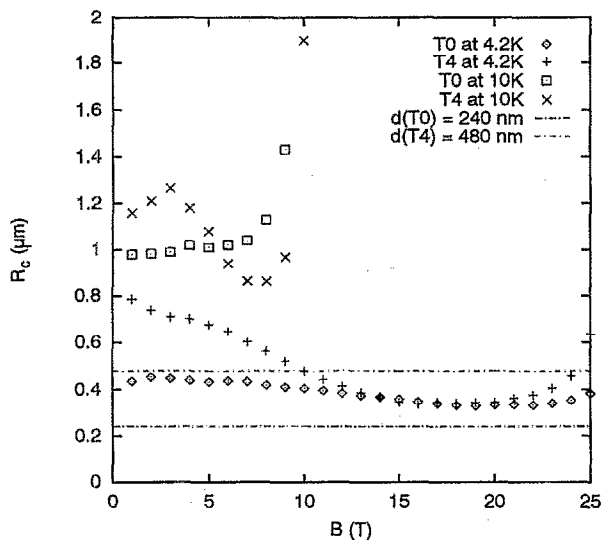Bonney, Willis, and Larbalestier   6385

FIG. 13. Critical length scale R_c, calculated from collective pinning theory, plotted as a function of applied field at 4.2 and 10 K. R_c varies only weakly with field and is, at 4.2 K, comparable to and, at 10 K, larger than the size of most grains in these samples.
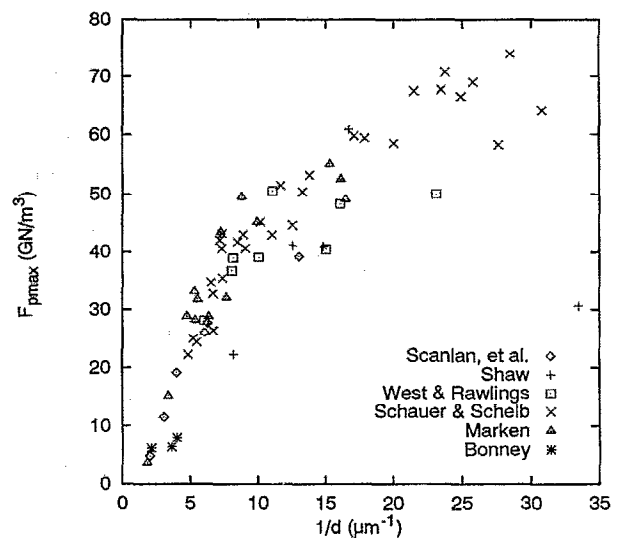

FIG. 14. $F_{p_{max}}$ (4.2 K) vs inverse average grain size for Nb$_3$Sn (see Refs. 28 and 33–37) and SMS. Values for SMS fall on the same curve suggesting that further reduction of SMS grain size will result in greater pinning forces.

but the effects of collective pinning by intragranular defects become apparent when d is larger and when R_c is relatively large at lower temperatures. These predictions are consistent with the present data.

D. Implications for further raising the J_c of SnMo$_6$S$_8$

In the present experiments we found that the flux pinning at higher fields was insensitive to quite aggressive heat treatments, while being sensitive at lower fields. Within the limited thermal treatment experiments that we conducted, it appeared that the only flux pinning defect which we varied significantly was the grain boundary density. The signature of its pinning was in all samples, as was that of a second type of defect, whose influence was felt preferentially at higher fields. As already discussed, we believe that this pinning was produced by planar intragranular defects. The cause of the planar intragranular defects is unknown. These defects must accommodate some lattice strain, the source of which is unclear. Lattice strain may be intrinsic to the SnMo$_6$S$_8$ crystal structure, or it may result from local stoichiometry fluctuations or from substitution of oxygen into the lattice. Local variations in chemistry could result in local variations in superconducting properties which could explain their pinning effect. If these defects simply resulted from HIP-induced strain, then we might expect that they would have annealed to lower density during the post-HIP annealing treatments. We did not observe this to occur. It is reasonable to expect that their density may be increased through doping or applied uniaxial strain. Because they potentially affect higher field J_c, optimization of intragranular defects appears to be particularly desirable. A factor of 3 enhancement of J_c was produced by Rossel and Fischer in PbMo$_6$S$_8$ through neutron irradiation;[9] those J_c values were only ~1/3 of the best val-

ues reported here. They also studied the influence of the addition of fine inert particles on CP J_c, but this gave less positive results on J_c.[9]

In Nb$_3$Sn samples there is a consistent dependence of the J_c on the inverse grain size ($1/d$) which is equivalent to the grain boundary length per unit area (L_{gb}). Figure 14 plots data sets from multiple authors on the relationship between $F_{p_{max}}$ (4.2 K) [the maximum value of $F_p(B)$] and $1/d$.[28,33–37] For inverse grain sizes between ~2 and 30 μm^{-1}, $F_{p_{max}}$ rises from ~5 to 75 GN/m^3. The data for our SMS samples fit into the extreme left hand corner of the plot, F_p lying between 6 and 8 GN/m^3 for values of $1/d$ ranging from 2 to 4 μm^{-1}. This plot strongly implies that the grain boundary flux pinning strength would be considerably stronger if the grain size could be substantially reduced. The Nb$_3$Sn data sets in Fig. 14 refer to data in the field range 4–6 T at 4.2 K, that is ~0.2b. According to the detailed study of Ochiai and Osamura,[21] grain size continues to play a role in determining the J_c at fields at least up to 15 T, which is ~0.7b. Thus, in addition to whatever contributions intragrain pinning can make, it also seems vital to continue to refine the grain size of CP compounds as an important step to raising the J_c at fields of order 20 T and higher.

Obtaining finer grain sizes is the subject of ongoing study by a number of routes. Grain size can be controlled through the processing parameters of temperature, time, and pressure. Smaller grain size may be obtained through lower-temperature HIP'ing and/or by forming the CP phase by reacting Pb and Sn with fine-grained Mo$_6$S$_8$ powders.[38] These methods for reducing CP grain size are compatible with wire formation techniques. We are, therefore, optimistic that finer-grained CP wires will soon be produced resulting in higher J_c CP conductors.

It is interesting that the more aggressive thermal treatments led to material with depressed low-field J_c values but with high-field J_c as great as that of the best sample. The

Bonney, Willis, and Larbalestier

ability to produce samples with a depressed low-field J_c, while maintaining high-field J_c values, also has value in engineering fusion or accelerator magnet conductors with minimal ac losses.

V. CONCLUSIONS

We found that HIP'ed $SnMo_6S_8$ samples exhibit critical current densities limited by insufficient flux pinning, not by granularity. That $B_{irr}(T) \sim B_{c_2}(T)$ indicates that flux pinning is strong and that these materials are not limited by flux creep. Systematic study of the microstructural dependence of J_c showed that J_c is controlled by grain boundary pinning at lower fields ($\leqslant 10$ T). However, J_c remains nearly constant with grain size above 15 T. Intragranular defects are believed to control the higher field pinning as grain boundary pinning declines. The observation of two distinct peaks in $F_p(B,T)$ is consisted with two pinning mechanisms acting to control J_c. Comparison of $SnMo_6S_8$ and Nb_3Sn pinning forces makes it clear that further reduction of CP grain size should increase J_c. To reduce d, lower processing temperatures and HIP processing are required. Increasing the density of intragranular defects should also enhance J_c preferentially at higher fields.

ACKNOWLEDGMENTS

[1] W. Goldacker, W. Specking, F. Weiss, G. Rimikis, and R. Flükiger, Adv. Cryo. Eng. 36, 353 (1990).
[2] B. Seeber, M. Decroux, and Ø. Fischer, Physica B 155, 129 (1989).
[3] Y. Kubo, F. Uchikawa, S. Utsunomiya, K. Noto, K. Katagiri, and N. Kobayashi, Cryogenics 33, 883 (1993).
[4] C. Rossel, E. Sandvold, M. Sergent, R. Chevrel, and M. Potel, Physica C 165, 233 (1990).
[5] D. Cattani, J. Cors, M. Decroux, and Ø. Fischer, IEEE Trans. Mag. 27, 950 (1991).
[6] H. Yamasaki, M. Umeda, S. Kosaka, Y. Kimura, T. C. Willis, and D. C. Larbalestier, J. Appl. Phys. 70, 1606 (1991).

[7] L. Le Lay, T. C. Willis, and D. C. Larbalestier, Appl. Phys. Lett. 60, 775 (1992).
[8] V. R. Karasik, M. O. Rikel', T. G. Togonidze, and V. I. Tsebro, Sov. Phys. Solid State 27, 1889 (1985).
[9] C. Rossel and Ø. Fischer, J. Phys. F Metal Phys. 14, 455 (1984).
[10] D. Cattani, R. Baillif, B. Seeber, Ø. Fischer, and W. Glätzle, in Proceeding of the 9th International Conference on Magnet Technology, edited by C. Marinucci and P. Weymuth (Swiss Institute for Nuclear Research, Villigen, Switzerland, 1985), p. 560.
[11] L. Le Lay, T. C. Willis, and D. C. Larbalestier, IEEE Trans. Mag. 27, 954 (1991).
[12] D. G. Hinks, J. D. Jorgensen, and H.-C. Li, Solid State Commun. 49, 51 (1984).
[13] D. W. Capone II, R. P. Guertin, S. Foner, D. G. Hinks, and H. C. Li, Phys. Rev. B 29, 6375 (1984).
[14] W. Goldacker, E. Seibt, G. Rimikis, and R. Flükiger, in Proceedings of the International Conference from Modern Super-conductivity towards Applications (ICMAS-90), edited by R. Tournier and R. Suryanarayanan, Technology Transfer Series, edited by A. Niku-Lari (IITT International, Paris, 1990), p. 99.
[15] L. A. Bonney, T. C. Willis, and D. C. Larbalestier, IEEE Trans. Appl. Superconductivity 3, 1582 (1993).
[16] E. J. Kramer, J. Appl. Phys. 44, 1360 (1973).
[17] Data fit by Peakfit™ which is distributed by Jandel Corp.
[18] M. Suenaga, A. K. Ghosh, Youwen Xu, and D. O. Welch, Phys. Rev. Lett. 66, 1777 (1991).
[19] M. Suenaga, D. O. Welch, and R. Budhani, Supercond. Sci. Technol. 5, S1 (1992).
[20] C. Rossel, O. Peña, H. Schmitt, and M. Sergent, Physica C 181, 363 (1991).
[21] S. Ochiai and K. Osamura, Acta Metall. 34, 2425 (1986).
[22] E. J. Kramer, J. Electronic Mater. 4, 839 (1975).
[23] E. J. Kramer, J. Appl. Phys. 44, 1360 (973).
[24] T. Matsushita and H. Küpfer. J. Appl. Phys. 63, 5048 (1988).
[25] H. Küpfer, R. Meier-Hirmer, and W. Schauer, Adv. Cryo. Eng. 34, 725 (1988).
[26] W. Goldacker, G. Rimikis, E. Seibt, and R. Flükiger, IEEE Trans. Mag. 27, 1779 (1991).
[27] S. A. Alterovitz and J. A. Woollam, Philos. Mag. B 38, 619 (1978).
[28] R. M. Scanlan, W. A. Fietz, and E. F. Koch, J. Appl. Phys. 46, 2244 (1975).
[29] M. Suenaga and D. O. Welch, in Filamentary A15 Superconductors, edited by M. Suenaga and A. Clark (Plenum, New York, 1980), p. 131.
[30] R. Wördenweber, Phys. Rev. B 46, 3076 (1992); Cryogenics 32, 1098 (1992).
[31] A. I. Larkin and Yu. N. Ovchinnikov, J. Low Temp. Phys. 34, 409 (1979).
[32] R. Scanlan, W. A. Fietz, and E. F. Koch, J. Appl. Phys. 46, 2244 (1975).
[33] B. J. Shaw, J. Appl. Phys. 47, 2143 (1976).
[34] A. W. West and R. D. Rawlings, J. Mater. Sci. 12, 1862 (1977).
[35] W. Schauer and W. Schelb, IEEE Trans. Mag. MAG-17, 374 (1981).
[36] K. Marken, Ph.D. thesis, University of Wisconsin-Madison, 1986.
[37] L. A. Bonney, Ph.D. thesis, University of Wisconsin-Madison, 1994.
[38] M. Decroux, P. Selvam, J. Cors, B. Seeber, Ø. Fischer, P. Rabiller, and R. Chevrel, IEEE Trans. Appl. Supercond. 3, 1502 (1993).

J. Appl. Phys., Vol. 77, No. 12, 15 June 1995

Bonney, Willis, and Larbalestier   6387